Universal scalable characterization and correction of pulse distortions in controlled quantum systems

Liang-Liang Guo,[1,2] Peng Duan,[1,2,*] Sheng Zhang,[1,2] Xin-Xin Yang,[1,2] Chi Zhang,[1,2] Lei Du,[1,2] Hai-Feng Zhang,[1,2] Hao-Ran Tao,[1,2] Tian-Le Wang,[1,2] Zhi-Long Jia,[1,2,3] Zhao-Yun Chen,[4,†] and Guo-Ping Guo[1,2,3,‡]

[1] *Chinese Academy of Sciences (CAS) Key Laboratory of Quantum Information, University of Science and Technology of China, Hefei, Anhui 230026, China*

[2] *CAS Center for Excellence and Synergetic Innovation Center in Quantum Information and Quantum Physics, University of Science and Technology of China, Hefei, Anhui 230026, China*

[3] *Origin Quantum Computing Company Limited, Hefei, Anhui 230088, China*

[4] *Institute of Artificial Intelligence, Hefei Comprehensive National Science Center, Hefei, Anhui 230088, China*

(Received 19 April 2023; revised 13 May 2024; accepted 21 May 2024; published 26 June 2024)

In quantum computation, control signals are adversely affected by distortion due to nonidealities in control chains. In order to implement high-fidelity digital and analog quantum operations, one must characterize the distortion and compensate for it. Here, we propose and experimentally verify an extensible method to model the behavior of control lines with the system function and correct it with digital filters. We correct the distortion of the superconducting-qubit flux control lines within a precision of 1×10^{-3}, which ensures gate fidelity free of the limit of pulse distortion. For the purpose of more accurate and scalable parameter extraction of the low-temperature line response, we employ an optimization-based protocol and the convergence is fast by setting the result of adjacent control lines with the same setup as the initial values. The techniques presented here improve distortion calibration efficiency and enable distortion-free operations, which paves the way for high-precision control of quantum computation and quantum simulation.

DOI: 10.1103/PhysRevApplied.21.064060

I. INTRODUCTION

Quantum computers have the potential to perform calculations that are classically intractable [1–3]. In order to achieve the full promise of quantum computing, it is necessary to advance state-of-the-art devices by pursuing improvements in the quality and efficiency of operations while scaling up the quantum processor size.

Among various quantum platforms, qubit manipulations are implemented by signals at different frequencies [4]. Microwave and base-band pulses are common in superconducting [5] and semiconductor spin qubits [6], while lasers are often used for trapped-ion [7] and neutral-atom qubits [8]. Due to imperfections in pulse generation and transmission, these signals have been distorted when arriving at qubits, which gives rise to control errors. In terms of single-qubit gates, microwave distortion can lead to under- and over-rotations as well as phase error [9,10]. For two-qubit gates, such as the controlled-phase gate, short-time-scale distortion can cause deviation from the carefully shaped trajectory, which contributes to leakage away from the computational subspace [11–15]. Moreover, the bleed-through [16,17] due to long-time-scale distortion makes the performance of the gate depend on the pulses applied historically. Therefore, compensating for distortion is crucial for achieving high-fidelity quantum operations.

We can regard qubit control lines as linear and time-invariant (LTI) systems. Common methods for describing LTI systems are the unit step response, the frequency response, and the system function [18]. The first two have already been used to characterize the distortion of qubit control lines [9,19–23]. However, this is time consuming if we want to measure short-time and long-time distortion comprehensively, which is impractical to scale up [21,24]. Deconvolution [23] is the traditional method to correct distortion, which requires the determination of the complete quantum circuit in advance, which is incompatible with feedback-based control.

Here, we first set up a universal model based on the system function to successfully describe the behavior of qubit control chains. We show that a few zeros and poles of the system function are sufficient to explain the response of

*Corresponding author: pengduan@ustc.edu.cn
†Corresponding author: chenzhaoyun@iai.ustc.edu.cn
‡Corresponding author: gpguo@ustc.edu.cn

various lines. Then, we use digital filters to predistort the desired pulse and the coefficients of the digital filter can be obtained directly from the reciprocal of the system function. Compared to the deconvolution method, corrections using a digital filter perform faster and can be carried out in real time when integrated into the field-programmable gate array (FPGA) [16,25,26].

We apply our methods to characterize and correct the distortion of flux control lines in superconducting quantum computation [20,21]. We first use the system function to fit the response of the instruments at room temperature and correct it to a level approaching the hardware limit. Then, a closed-loop-optimization approach [17] is utilized to extract the parameters of the control wiring at low temperature. This optimization aims to make the qubit fidelity independent of previous pulses and is thus independent of details of the qubit. We use the calibration parameters of one qubit control as the initial value for calibrating the next qubit, with nominally identical control lines, in the same manner. This accelerates the convergence speed and thus the optimization-based approach is scalable to large-scale processors. The inaccuracy of correction is verified to be 1×10^{-3}, which is comparable to the current state-of-the-art level [20]. Given that the system function is a general description of LTI systems, the methods proposed here are applicable to other frequency ranges and platforms that are also influenced by distortion [9,19].

II. CHARACTERIZATION AND CORRECTION OF DISTORTION USING THE SYSTEM FUNCTION AND DIGITAL FILTER

In mathematics and signal processing, the z transform converts a discrete-time signal, which is a sequence of real or complex numbers, into a complex frequency-domain (the z-domain) representation [27]. This can be considered as a discrete-time equivalent of the Laplace transform (the s domain) [28].

For an LTI system, the impulse response $h(n)$ encodes all the information required to process an arbitrary input signal $x(n)$ into an output signal $y(n)$. The mathematical operation is denoted by $y(n) = h(n) * x(n)$, where the asterisk ("$*$") indicates convolution and the variable n is integer valued and represents discrete instances in time. We can represent the input-output relation in the z domain by $Y(z) = H(z)X(z)$, where $X(z)$, $Y(z)$, and $H(z)$ are the z transform of $x(n)$, $y(n)$, and $h(n)$, respectively.

$H(z)$ is called the system function and can generally be written as a rational function,

$$H(z) = \frac{B(z)}{A(z)} = \frac{\sum_{m=0}^{M} b_m z^{-m}}{1 + \sum_{n=1}^{N} a_n z^{-n}} = b_0 z^{N-M} \frac{\prod_{m=1}^{M} (z - z_m)}{\prod_{n=1}^{N} (z - p_n)}, \quad M \geq N, \tag{1}$$

where $B(z)$ and $A(z)$ are the numerator and denominator polynomials in z^{-1}. They are defined by the polynomial coefficients b_m (a_n) and the polynomial degree M (N). p_n and z_m are called poles and zeros of the system, respectively. If $H(z)$ is used to model digital filters, b_m and a_n are called filter-tap coefficients, where M and N are the feedforward and feedback filter orders, respectively.

By performing partial fraction expansion, we obtain

$$H(z) = H_0(z) + \sum_{l=1}^{L} C_{1,l} H_{1,l}(z) + \sum_{k=1}^{K} C_{2,k} H_{2,k}(z), \tag{2}$$

where

$$H_0(z) = \sum_{s=0}^{M-N} C_{0,s} z^{-s}, \tag{3a}$$

$$H_1(z) = \frac{1 - p_1}{1 - p_1 z^{-1}}, \tag{3b}$$

$$H_2(z) = \frac{r e^{j\varphi_r}}{1 - p_2 e^{j\varphi_p} z^{-1}} + \frac{r e^{-j\varphi_r}}{1 - p_2 e^{-j\varphi_p} z^{-1}}, \tag{3c}$$

$$N = L + 2K. \tag{3d}$$

Here, $H_0(z)$ is a polynomial term that describes the *finite-duration impulse response* (FIR) behavior and $C_{0,s}$ is the polynomial coefficient. The remaining proper rational parts in Eq. (2) are related to the *infinite-duration impulse response* (IIR) behavior. $H_1(z)$ contains a real pole p_1 and $H_2(z)$ contains a pair of complex-conjugate poles, $p_2 e^{j\varphi_p}$ and $p_2 e^{-j\varphi_p}$. When the poles appear as complex-conjugate pairs, their residues will also be complex conjugates denoted by $r e^{j\varphi_r}$, $r e^{-j\varphi_r}$. L is the number of real poles and K is the pair of complex poles. $C_{1,l}$ and $C_{2,k}$ are the proportion coefficients of the corresponding terms.

The unit step response is the system response to the unit step function and the derivative of the unit step response is the impulse response. We can derive the continuous-time unit step response $y_u(t)$ from Eq. (2) (for a detailed derivation, see Appendix B). When $t \geq 0$,

$$y_u(t) = \sum_{s=0}^{M-N} C_{0,s} u(t/T_0 - s) + \sum_{l=1}^{L} C_{1,l}(-p_{1,l} e^{-t/\tau_{1,l}} + 1) + \sum_{k=1}^{K} C_{2,k} \left[2A_k e^{-t/\tau_{2,k}} \cos(2\pi t/T_k + \varphi_k) + 1\right], \tag{4}$$

where $\tau_1 = -T_0/\ln p_1$, $\tau_2 = -T_0/\ln p_2$, $T = 2\pi T_0/\varphi_p$, and $A e^{j\varphi} = (r\cos\varphi_r - (1/2)) - j[(2r\cos\varphi_r - 1)\cos\varphi_p + p_2]/(2\sin\varphi_p)$. $u(t)$ is the unit step function and the quantity T_0 is the sampling interval.

In previous reports [21,29–31], the sum of exponentials is often used to fit the measured unit step response and

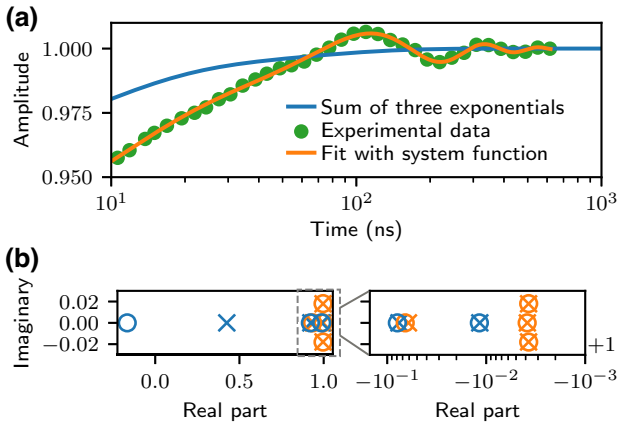

FIG. 1. Two methods to describe LTI systems. (a) The unit step response of different control lines: the legend is valid for all subplots. The green circle is the response sampled during the experiment and the orange line is the fitting result with Eq. (4). (b) The pole-zero plot, where × indicates poles and the circle indicates zeros.

Eq. (4) indicates that it just corresponds to the real-poles term. The system function is a more generalized model in which additional complex poles are related to decaying oscillations and the polynomial term can represent FIR behavior.

In Fig. 1, we present a comparison of describing line responses with the unit step response and the system function (the pole-zero plot). When using the system function, we only need a few zeros and poles in the complex plane instead of a continuous curve in the time or frequency domain. The sum of the exponential response is a typical response of the control lines that transmit baseband pulses. As displayed in Fig. 1(b), these exponential responses are represented by real poles and zeros. The green circle in Fig. 1(a) is the response acquired in our experimental system. The sum of exponentials is unable to perform the fitting but Eq. (4) with $L = 2$ and $K = 1$ is competent. The oscillation in the response consists with the complex-conjugate poles and zeros in Fig. 1(b).

In order to compensate for the distortion, we use digital filters to predistort the desired pulse. It is not an easy task to design a digital filter directly from the time-domain or frequency-domain response. Fortunately, the system function can be employed not only to model the response of various LTI systems but also to conveniently generate a predistortion digital filter.

Evidently, the digital filter is required to satisfy $H_{\text{inv}} = 1/H(z)$ and we only need to exchange the numerator and denominator coefficients of the system function to obtain filter taps. A high-order digital filter is at the risk of numerical precision errors; therefore, we convert it to a series of second-order filters with a direct-form II transposed structure [32]. Considering the limited bandwidth of the arbitrary wave-form generator (AWG) and the need to prevent overshoot, we also add a Gaussian FIR low-pass filter with a cutoff frequency of 230 MHz in the predistortion module.

III. EXPERIMENTS

We apply the new characterization and correction scheme to the flux control lines of superconducting qubits. The quantum processor used here is a tunable-coupling structure [14,31,33–35], similar to our sample in Ref. [36]. We call the two qubits used Q1 and Q2. The AWG used for fast flux control features a 1.6-Gsamples/s, sample rate and a 14-bit vertical resolution. The dc and fast flux control signals are combined using a customized dc bias tee [30,37,38], which is the source of the complex poles due to the large inductance and stray capacitance. A detailed experimental wiring setup and room-temperature electronics can be found in Appendix A.

A. Room-temperature electronics correction

The compensation of distortion consists of two steps and we first calibrate the room-temperature hardware using an oscilloscope. The uncorrected response in Fig. 2 is the result sampled at the output of the AWG channel and the setting time is longer than 30 μs. We use Eq. (4) to heuristically implement IIR fitting and temporarily consider a constant coefficient $C_{0,0}$ for the FIR term. In Fig. 2(c), we show the fitting result with $L = 4, 5, 6$; five real poles is optimal. Complete FIR terms with a length of 20 ns

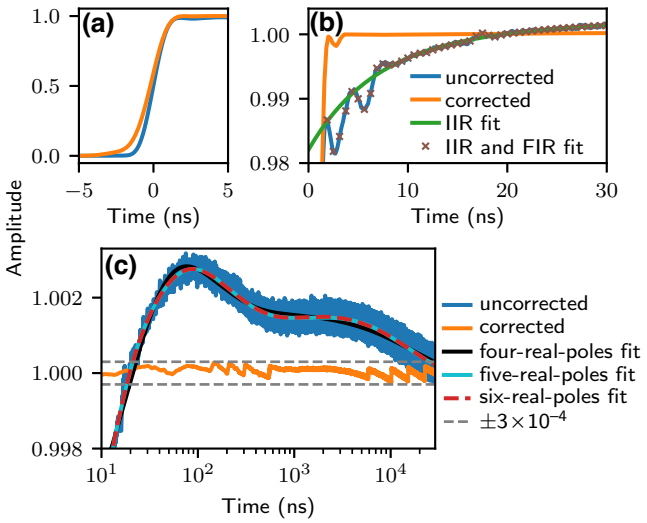

FIG. 2. The unit step response of the AWG with or without correction. (a) The rising edge of the response. The rise time after correction increases slightly because of the use of the Gaussian FIR digital filter. (b),(c) The (b) short- and (c) long-time-scale response. We fit the uncorrected response and Eq. (4) with five real poles is adequate to fit the IIR behavior well. The response after correction is smoothed with a moving-average filter.

are determined using the residual between the sampled response and the IIR fitting. The IIR and FIR fitting displayed in Fig. 2(b) interprets the AWG response perfectly. We generate a digital filter to calibrate the output response of the AWG and the result is shown as the orange line in Fig. 2. The saw-tooth nature of Fig. 2(c) results from the limited 14-bit vertical resolution of the AWG; the influence is decreased in the following experiments by using pulses with larger amplitude.

B. Low-temperature lines correction

We then utilize qubits to characterize the distortion of the low-temperature lines. For each qubit, we select a flux-sensitive working point and implement regular calibration to obtain a high-fidelity single-qubit gate when no flux pulse is applied on the Z line. We begin by measuring the unit step response of the flux control line of Q1 [39] (for a detailed test method and raw data, see Appendix C). The response is fitted well with one real pole, a pair of complex poles, and a single FIR coefficient $C_{0,0}$. The red line in Fig. 3(c) is the fitting result and the corresponding parameters are listed in Table I.

Next, we utilize closed-loop optimization [40] to obtain these parameters more accurately and we show the control sequence in Fig. 3(a). We play a randomized-benchmarking (RB) sequence on the X-Y line [41,42]. On the Z line, we apply a fixed-duration (200-ns) square pulse. Left uncompensated [see the red dashed line in Fig. 3(a) for illustration], the tail of the square pulse will bring the frequency of the qubit away from its working point where single-qubit gates are calibrated and cause the RB result to become terrible. We now generate a digital filter directly from the system-function parameters to predistort the square pulse. The distortion can be perfectly calibrated only if these parameters are optimized to accurately model the flux line. As a result, the square pulse after correction does not influence the RB sequence. The idle point of the qubit is 256 MHz below the sweet spot and the single-qubit gate is implemented by the derivative removal by adiabatic gate (DRAG) method [10,43] with a 20-ns cosine envelope and a 5-ns pad. The wait time τ between the square pulse and the RB sequence is 5 ns, ensuring that the potential FIR behavior vanishes.

The optimization algorithm is the Nelder-Mead simplex [44] and the cost function is the average fidelity of k different RB sequences at fixed length m. Here, we set m and k to 50 and 30, respectively. The total duration of the RB sequence is approximately 3 μ s and one can increase the value of m if there is distortion with a longer time constant. We start the optimization by using the fitting parameters listed in Table I as the initial values. The optimization process is illustrated in Fig. 3(b) and converges on optimal parameters after about 70 function evaluations. The optimization result is also shown in Table I.

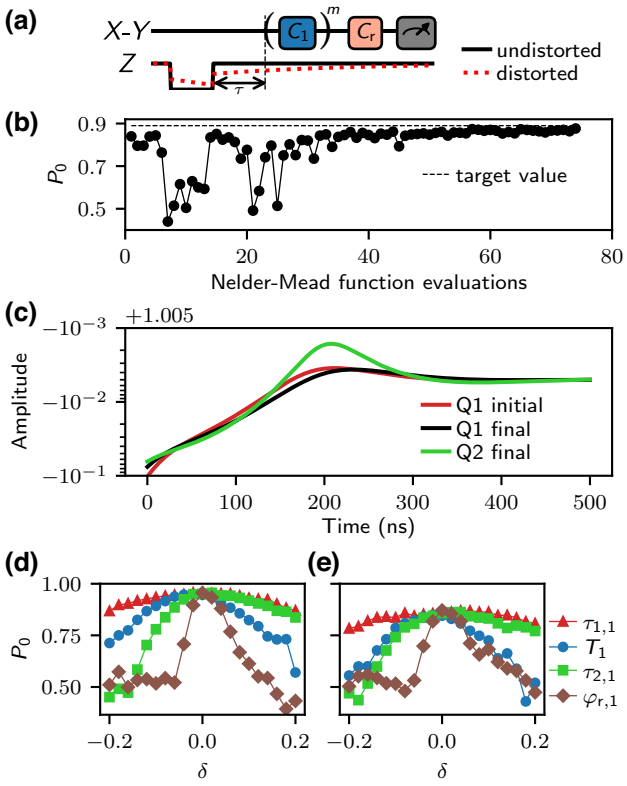

FIG. 3. The determination of the low-temperature line response using closed-loop optimization. (a) The pulse sequence used to optimize the system-function parameters. On the X-Y line, we play a sequence of Clifford gates with length m, appended by recovery Clifford gates C_r that make the ideal operation the identity. We define the sequence fidelity as the ground-state population (P_0). (b) The change of the sequence fidelity at $m = 50$ versus the number of evaluations. The optimization converges to the target value, which is the fidelity of the RB sequence at $m = 50$ when no flux pulse is applied on the Z line. (c) The unit step responses correspond to the parameters listed in Table I. Variations between control lines with the same setup are indeed small. (d),(e) The sensitivity analysis of selected parameters for (d) $m = 1$ and (e) $m = 50$. δ is the deviation fraction of the parameters from their optimum.

There is a target value for the convergence in Fig. 3(b), which is the fidelity of the RB sequence at the same m as we select for the optimization but with no flux pulse applied on the Z line. When we apply a square pulse on the Z line to implement the optimization, the degradation of the sequence fidelity compared with this target value arises solely from the tail of the square pulse due to distortion. In Fig. 3(b), the optimization converges to this target value, which indicates that the distortion of the square pulse applied on the Z line is successfully compensated for and has no effect on the subsequent RB sequence.

In Figs. 3(d) and 3(e), we measure the sequence fidelity at $m = 1$ and 50 as we vary each of the system-function parameters from their optimum values. The sequence

TABLE I. The system-function parameters before and after closed-loop optimization; the corresponding responses are plotted in Fig. 3(c).

	$C_{0,0}$	$C_{1,1}$ (%)	$\tau_{1,1}$ (ns)	$C_{2,1}$ (%)	T_1 (ns)[a]	$\tau_{2,1}$ (ns)	$\varphi_{r,1}$
Q1 initial	0.900	8.81	19.3	1.19	354.2	66.2	0.95
Q1 final	0.928	6.12	22.1	1.08	387.0	68.3	0.93
Q2 final	0.940	4.73	27.2	1.27	337.0	83.9	0.84

[a]This value does not denote the qubit energy-relaxation time.

fidelity decreases because a slight deviation in the parameters can cause the digital filters to become unable to correct the distortion. This effect is more sensitive to parameters that affect long-time-scale distortion and increasing m may further increase the sensitivity.

Note that for the initial value of the optimization, we sample the unit step response only for the first measured qubit on the processor. The remaining qubits directly employ the optimization result of the adjacent qubit as their initial value. This is reasonable because the differences between the control lines with the same setup are small. Based on the optimization result of Q1, we obtain the system-function parameters of Q2, which can be seen in Table I.

C. Residual response after room-temperature and low-temperature distortion corrections

In Fig. 4(a), we summarize the two-step procedure for correcting the distortion of the qubit flux control lines. Digital filters $\tilde{H}_{\mathrm{RT}}^{-1}$ and $\tilde{H}_{\mathrm{LT}}^{-1}$ are used to compensate for the room-temperature response H_{RT} and the low-temperature response H_{LT}, respectively. The Gaussian FIR low-pass filter H_G is used to account for the limited bandwidth of the AWG and to prevent overshoot. Ideally, the response after correction will approach the response of the Gaussian FIR filter H_G. In Figs. 4(b) and 4(c), we plot the remnant response of Q2 sampled using the cryoscope method [20] and the distortion is corrected to within 10^{-3}. Successful correction of Q2 also indicates the reliability of taking advantage of the parameters of the adjacent qubit as the initial value. Hence, closed-loop optimization will speed up the full characterization of the low-temperature line distortion on a large-scale processor (for a summary of the steps to implement the optimization-based method and a comparison between the optimization-based method and existing methods [23,36], see Appendix D 2).

The traditional method for distortion correction is the deconvolution method [23], which is briefly introduced in Appendix D 1. We evaluate the run times of the two predistortion schemes as the length of the wave form to be compensated increases. The run time here refers to the execution time for the predistortion calculation of the wave form on our laptop and the same computer configurations are maintained when we conduct the comparison. The results are shown in Fig. 4(d). We use the digital filter and unit step response of Q1 to implement the test. The unit step response is truncated to 500 ns for the deconvolution calculation. Because digital filters only involve linear operations, the run time of the predistortion calculation increases linearly with the length of the wave form. The digital-filter-based predistortion method takes only 1% of the time required by the deconvolution method. This highlights the advantage of using digital filters for predistortion, as they offer significant speedups over deconvolution methods, especially for long wave forms. Fast wave-form predistortion is essential for the efficient operation of quantum algorithms, especially when

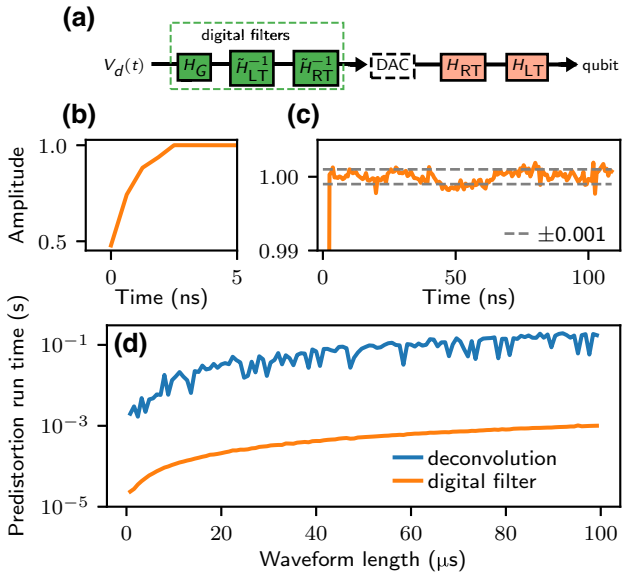

FIG. 4. The residual response after distortion correction. (a) A schematic of the predistortion procedure. The desired pulse $V_d(t)$ is predistorted by digital filters before being sent to a digital-to-analog converter (DAC), then transmitted through control lines, and finally arrives at the qubit. (b),(c) The (b) short- and (c) long-time-scale residual responses after distortion correction. The unit step response is sampled using the cryoscope method [20] and the distortion is corrected to the range within 10^{-3}. (d) A comparison of the calculation times between the two predistortion schemes. The digital filter comprises linear operations, whereas deconvolution involves Fourier-transform and inverse-Fourier-transform operations.

the number of qubits is large and the quantum circuit is long.

IV. CONCLUSIONS

In conclusion, we propose a universal approach for accurate distortion characterization and correction based on the system function and digital filtering. We experimentally verify the performance of our approach by employing the protocol to calibrate the flux control lines of superconducting qubits. We observe that the distortion is corrected within a precision of 10^{-3} after room-temperature and low-temperature calibration. Microwave-pulse distortion is also observed in experiments [9,45,46] and is often mitigated by placing a short idle time between gates [47]. The protocol described here can also be used to calibrate the distortion of microwave control lines.

Improvements in calibration efficiency and extensibility are crucial when processors scale up. The optimization-based method introduced to extract the parameters of the low-temperature line response significantly improves the calibration speed. Setting times as long as 10 μs are observed [21,31] and one only needs to increase the length of the RB sequence in our method to characterize it quickly, without increasing the test time. The weakness of this method is the reduced sensitivity to short-time distortion (approximately 20 ns) but it can be verified using the cryoscope method. If there is a survival response, one could add additional FIR filters to deal with it.

The digital filter outperforms the deconvolution method in terms of speed, especially when the distortion or sequence is long. Here, we implement the digital filter in software, which requires significant wave-form memory and prior knowledge of all the operations required by a quantum circuit. Alternatively, one can integrate the digital filter into the FPGA to achieve real-time predistortion, which is essential for feedback control. Our techniques reduce the time required for calibrating distortion and promise a distortion-free signal, which would simplify the calibration process of processors, benefit higher-fidelity operations, and ultimately enhance the performance of algorithms and simulations executed on quantum processors.

ACKNOWLEDGMENTS

This work was supported by the National Natural Science Foundation of China (Grants No. 12034018 and No. 11625419). This work was partially carried out at the University of Science and Technology of China (USTC) Center for Micro and Nanoscale Research and Fabrication.

APPENDIX A: EXPERIMENTAL SETUP

The experimental wiring setup and room-temperature electronics are shown in Fig. 5.

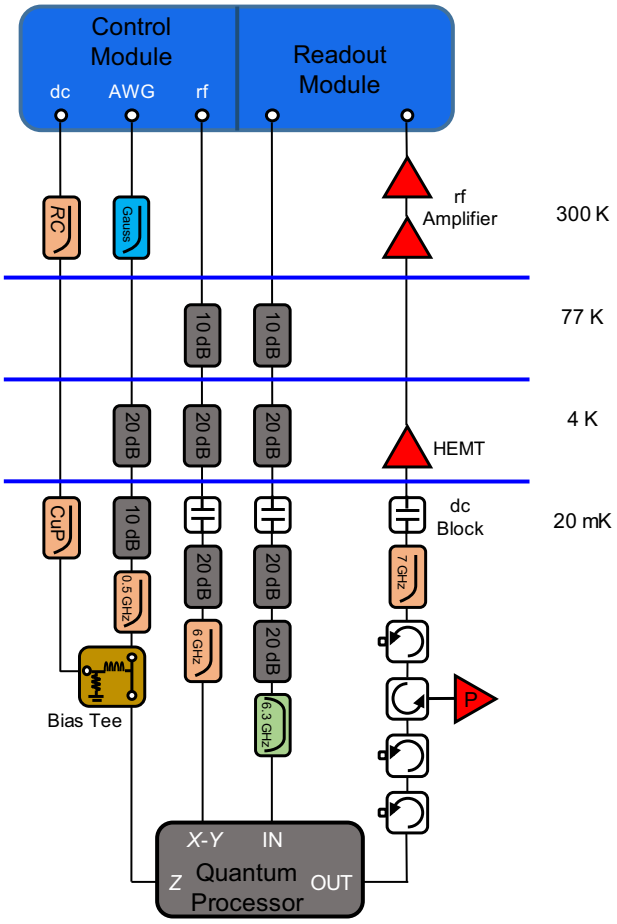

FIG. 5. The full wiring diagram of the experimental setup. The experimental wiring setup and quantum control system are developed jointly with OriginQ, Inc. The customized dc bias tee removes the capacitor and comprises a 6.7-μH conical inductor and a grounded 50-Ω resistor at the dc port.

APPENDIX B: DERIVATION OF THE UNIT STEP RESPONSE FROM THE SYSTEM FUNCTION

For an LTI system, the system response $y(n)$ to an arbitrary input signal $x(n)$ is determined by the impulse response $h(n)$. The impulse response is the system response to a Dirac delta function. In general, it is not a trivial task to measure the impulse response directly, since it is impossible to generate an ideal Dirac delta function as an input in any real system.

An alternative method is the measurement of the step response $y_u(n) = h(n) * u(n)$, where $u(n)$ denotes the unit step function. In contrast to a Dirac delta function, the unit step function is better reproduced on an AWG, as it has a finite bandwidth. The impulse response can then be obtained by differentiation of the unit step response [23].

The system function $H(z)$ is the z transform of the impulse response $h(n)$ and can generally be written in the form of a rational fraction of z^{-1} [see Eq. (1)]. In this appendix, we will derive the general form of the unit

step response based on Eq. (1). After establishing the relationship between the system function and the unit step response, we can experimentally measure the unit step response and obtain the system function of the qubit control chain through parameter fitting. Then, the coefficients of the digital filter used to predistort the desired pulse can be obtained directly from the reciprocal of the system function.

The z transform of the unit step function $u(n)$ is

$$u(z) = \mathcal{Z}[u(n)] = \frac{1}{1-z^{-1}}. \tag{B1}$$

Here, $\mathcal{Z}[\cdot]$ and $\mathcal{Z}^{-1}[\cdot]$ represent the operator of z transform and the inverse z transform, respectively. We multiply $u(z)$ by the system function $H(z)$ in the z domain and an inverse z transform of the result will yield the unit step response $y_u(n)$.

We can obtain Eq. (2) by performing partial fraction expansion on the system function in Eq. (1). There are three kinds of components in Eq. (2), including a polynomial term [Eq. (3a)], terms with real poles [Eq. (3b)], and terms with complex poles [Eq. (3c)]. These terms correspond to different types of unit step responses, which we will derive separately in the following.

1. FIR response

$H_0(z)$ in Eq. (3a) is a polynomial of z^{-1}. We multiply $H_0(z)$ by $u(z)$ to obtain

$$Y_0(z) = H_0(z)u(z) = \sum_{s=0}^{M-N} C_{0,s} z^{-s} u(z). \tag{B2}$$

The z transform has the sample-shifting property $\mathcal{Z}[u(n-n_0)] = z^{-n_0}u(z)$ and the inverse z transform of $Y_0(z)$ yields

$$\begin{aligned} y_0(n) = \mathcal{Z}^{-1}[Y_0(z)] &= \sum_{s=0}^{M-N} C_{0,s}\mathcal{Z}^{-1}[z^{-s}u(z)] \\ &= \sum_{s=0}^{M-N} C_{0,s}u(n-s). \end{aligned} \tag{B3}$$

When $n \geq M-N$, $y_0(n)$ is a constant equal to $\sum_{s=0}^{M-N} C_{0,s}$. Therefore, $y_0(n)$ corresponds to a *finite-duration impulse response* (FIR) with a length of $M-N+1$.

2. IIR response

The remaining parts of Eq. (2), excluding the polynomial term, constitute the proper rational parts of $H(z)$. These parts are associated with another type of response, known as the *infinite-duration impulse response* (IIR).

By performing a partial fraction expansion on the proper rational part and dividing the result into two categories based on the pole being real or complex, we obtain $H_1(z)$ and $H_2(z)$. We normalize $H_1(z)$ and $H_2(z)$ by setting their values to 1 at $z=1$ and using $C_{1,l}$ and $C_{2,k}$ as the proportion coefficients of the corresponding terms.

a. Real poles

For $H_1(z)$ in Eq. (3b), it contains a real pole p_1. $H_1(1) = 1$ indicates that it has already been normalized. We multiply $H_1(z)$ by $u(z)$ to obtain

$$\begin{aligned} Y_1(z) = H_1(z)u(z) &= \frac{1-p_1}{(1-p_1z^{-1})(1-z^{-1})} \\ &= \frac{-p_1}{1-p_1z^{-1}} + \frac{1}{1-z^{-1}}. \end{aligned} \tag{B4}$$

The partial fraction expansion method is a practical approach for the inverse z-transform procedure that utilizes certain known z-transform pairs. Specifically, we have that $\mathcal{Z}^{-1}[\frac{1}{1-pz^{-1}}] = p^n u(n)$, where p denotes a constant. Therefore, the inverse z transform of $Y_1(z)$ is given by

$$y_1(n) = \mathcal{Z}^{-1}[Y_1(z)] = (-p_1^{n+1}+1)u(n). \tag{B5}$$

A causal LTI system is said to be bounded-input bounded-output (BIBO) stable if and only if all poles are inside the unit circle. As a result, $|p_1| < 1$. If $p_1 < 0$, $y_1(n)$ exhibits odd-even oscillations, which we do not consider here. When $0 < p_1 < 1$, $y_1(n)$ describes the exponential response.

b. Complex poles

For $H_2(z)$ in Eq. (3c), it contains a pair of complex-conjugate poles $p_2e^{j\varphi_p}$, $p_2e^{-j\varphi_p}$ and their residues are also complex conjugates, denoted by $re^{j\varphi_r}$ and $re^{-j\varphi_r}$.

Given the normalized condition, we obtain

$$H_2(1) = \frac{re^{j\varphi_r}}{1-p_2e^{j\varphi_p}} + \frac{re^{-j\varphi_r}}{1-p_2e^{-j\varphi_p}} = 1. \tag{B6}$$

We multiply $H_2(z)$ and $u(z)$, to obtain

$$\begin{aligned} Y_2(z) &= H_2(z)u(z) \\ &= \left(\frac{re^{j\varphi_r}}{1-p_2e^{j\varphi_p}z^{-1}} + \frac{re^{-j\varphi_r}}{1-p_2e^{-j\varphi_p}z^{-1}}\right)\frac{1}{1-z^{-1}} \\ &= \frac{m_1}{1-p_2e^{j\varphi_p}z^{-1}} + \frac{m_2}{1-p_2e^{-j\varphi_p}z^{-1}} + \frac{1}{1-z^{-1}}, \end{aligned} \tag{B7}$$

where

$$m_{12} = -\frac{(2r\cos\varphi_r - 1)\cos\varphi_p + p_2}{2\sin\varphi_p}, \tag{B8a}$$

$$m_1 = \left(r\cos\varphi_r - \frac{1}{2}\right) + jm_{12} = Ae^{j\varphi}, \tag{B8b}$$

$$m_2 = \left(r\cos\varphi_r - \frac{1}{2}\right) - jm_{12} = Ae^{-j\varphi}. \tag{B8c}$$

Taking the inverse z transform of Eq. (B7) yields

$$\begin{aligned} y_2(n) &= \mathcal{Z}^{-1}[Y_2(z)] = \left[m_1(p_2e^{j\varphi_p})^n + m_2(p_2e^{-j\varphi_p})^n + 1\right] \\ u(n) &= \left[2Ap_2^n\cos\left(\varphi_p n + \varphi\right) + 1\right]u(n). \end{aligned} \tag{B9}$$

We have $0 < p_2 < 1$ and $y_2(n)$ describes the decaying-oscillation response.

3. Complete response

By combining all the responses mentioned above, we obtain the complete unit step response stemming from the system function in Eq. (2):

$$\begin{aligned} y_u(n) &= \mathcal{Z}^{-1}[H(z)u(z)] \\ &= y_0(n) + \sum_{l=1}^{L} C_{1,l}y_{1,l}(n) + \sum_{k=1}^{K} C_{2,k}y_{2,k}(n) \\ &= \sum_{s=0}^{M-N} C_{0,s}u(n-s) + \sum_{l=1}^{L} C_{1,l}(-p_{1,l}^{n+1} + 1)u(n) \\ &\quad + \sum_{k=1}^{K} C_{2,k}\left[2A_kp_{2,k}^n\cos\left(\varphi_{p,k}n + \varphi_k\right) + 1\right]u(n). \end{aligned} \tag{B10}$$

$y_u(n)$ can be conveniently related to the continuous-time response $y_u(t)$ using an operation called sampling, in which $y_u(t)$ values at equally spaced points $t = nT_0$ are assigned to $y_u(n)$. The quantity T_0 is called the sampling interval. When $t \geq 0$,

$$\begin{aligned} y_u(t) &= \sum_{s=0}^{M-N} C_{0,s}u(t/T_0 - s) + \sum_{l=1}^{L} C_{1,l}(-p_{1,l}^{t/T_0+1} + 1) \\ &\quad + \sum_{k=1}^{K} C_{2,k}\left[2A_kp_{2,k}^{t/T_0}\cos\left(\varphi_{p,k}t/T_0 + \varphi_k\right) + 1\right] \\ &= \sum_{s=0}^{M-N} C_{0,s}u(t/T_0 - s) + \sum_{l=1}^{L} C_{1,l}(-p_{1,l}e^{-t/\tau_{1,l}} + 1) \\ &\quad + \sum_{k=1}^{K} C_{2,k}\left[2A_ke^{-t/\tau_{2,k}}\cos\left(2\pi t/T_k + \varphi_k\right) + 1\right], \end{aligned} \tag{B11}$$

where $\tau_1 = -T_0/\ln p_1, \tau_2 = -T_0/\ln p_2$ and $T = 2\pi T_0/\varphi_p$.

In summary, this appendix outlines a technique for obtaining the unit step response of an LTI system from its system function. Moreover, we have provided a comprehensive discussion on the various components of the unit step response, along with their respective properties. Specifically, the real poles are used to describe the exponential response, the complex poles are associated with the decaying-oscillation response, and the polynomial term signifies the FIR response.

APPENDIX C: TIME-DOMAIN CHARACTERIZATION OF LOW-TEMPERATURE LINE DISTORTION

As described in the main text, time-domain measurement is needed only for one of the lines once we change the setup of the flux control wiring and Fig. 6(a) shows the control sequence. We first calibrate a π pulse without applying a Z pulse to provide a high-fidelity $|0\rangle \rightarrow |1\rangle$ qubit transition. We then add a 1-μs square pulse with Z_{amp} amplitude on the flux control line and observe the second flank of the wave form. If uncompensated, the qubit frequency will be shifted due to the tail of the square pulse, which causes it to be hard for the calibrated π pulse to excite the qubit sufficiently. A flux bias offset ΔZ is added to compensate for the tail until the excitation induced by the π pulse can return to its original value. As shown in Fig. 6(b), the unit step response can be reconstructed by scanning the delay time and ΔZ and the result is shown as red dots in Fig. 6(c).

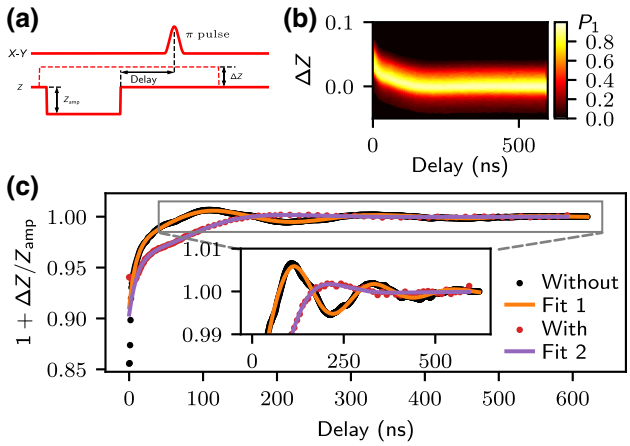

FIG. 6. The unit-step-response measurement of the flux control lines. (a) The pulse sequence used in this experiment. (b) We sweep the compensation amplitude ΔZ to make the π pulse recover its fidelity as we change the delay time. (c) The reconstructed unit step response and the system-function fit. We present the results for the bias tee with or without a grounded 50-Ω resistor.

A comparison of whether or not there is a grounded resistor at the dc port of the bias tee is displayed in Fig. 6(c) and both the experimental data are fitted by the system function. A grounded resistor changes the damping properties and causes the oscillation to decay more quickly.

APPENDIX D: SUMMARY AND COMPARISON OF DIFFERENT DISTORTION-CORRECTION AND CHARACTERIZATION METHODS

1. Deconvolution method

In the main text, we propose the use of digital filters to correct distortions. The traditional method for distortion correction is the deconvolution method, which will be briefly introduced below.

Because of imperfections in pulse generation and transmission, the control pulses arriving at the qubits are different from the wave form that we design. The mathematical operation is denoted by $y_{\text{qubit}}(n) = h(n) * x_{\text{in}}(n)$, where $x_{\text{in}}(n)$ represents our intended signal, $y_{\text{qubit}}(n)$ is the signal actually seen by the qubit, and $h(n)$ is the impulse response of the control chain. Convolution in the time domain corresponds to multiplication in frequency space, resulting in $Y_{\text{qubit}}(f) = H(f)X_{\text{in}}(f)$, where $Y_{\text{qubit}}(f)$, $H(f)$, and $X_{\text{in}}(f)$ are the Fourier transforms of $y_{\text{qubit}}(n)$, $h(n)$, and $x_{\text{in}}(n)$, respectively. Control pulses can be corrected by performing deconvolution, which involves multiplying our desired pulse with the inverse of $H(f)$ and taking the inverse Fourier transform of the result. This yields $x_{\text{corrected}}(n) = \mathcal{F}^{-1}[H^{-1}(f)X_{\text{in}}(f)]$. The operator $\mathcal{F}^{-1}[\cdot]$ represents the inverse Fourier transform. We send $x_{\text{corrected}}(n)$ as a predistortion input and the pulse arriving at the qubit is equivalent to the intended signal $x_{\text{in}}(n)$.

2. Characterization methods of low-temperature line distortion for a large number of qubits

a. Time-domain characterization method

The prevalent technique in the community for low-temperature control-line distortion characterization is time-domain measurement of the unit step response [20,21,23]. Either by employing the method described in Appendix C or utilizing the cryoscope approach, there will be discrepancies between the measurement result and the actual line response due to system errors in the schemes and experimental noise. To enhance the accuracy of the distortion correction, the residual response after predistortion is collected and employed for iterative calibration. The general steps involved are as follows:

(1) Conduct the measurement of the unit step response of the control chain and derive the impulse response $h(n)$ by taking the derivative of the unit step response.

(2) Upon obtaining the impulse response of the control chain $h(n)$, utilize the deconvolution method outlined in Appendix D 1 for distortion correction and collect the unit step response after correction, referred to as the residual response.

(3) Determine whether the residual response converges within the target range. If not, derive $h'(n)$ by taking the derivative of the residual response and update the impulse response of the control chain by convolving $h'(n)$ with $h(n)$.

(4) Repeat steps (2) and (3) several times until the residual response converges within a specific range, such as 10^{-3}.

To characterize the low-temperature line responses of multiple qubits in a large quantum processor, perform the above procedure sequentially for each qubit.

b. Optimization-based method

To some extent, the iterative calibration scheme in the time domain enhances the accuracy of the distortion calibration. However, it significantly increases the time required for distortion characterization due to the necessity of multiple measurements of the unit step response. Therefore, we suggest the optimization-based method proposed in the main text to extract the parameters of the low-temperature line response, which can improve the calibration speed. The work flow of the optimization-based method can be summarized as follows:

(1) For each qubit, select a flux-sensitive working point and implement regular calibration to obtain a high-fidelity single-qubit gate when no flux pulse is applied in the Z line.

(2) Set the initial value of the optimization based on the following principles. For the first measured qubit on a large processor, we measure the unit step response of the low-temperature line and obtain the initial value by fitting the response with Eq. (4). The remaining qubits directly employ the optimization result of an adjacent qubit as their initial value.

(3) For each qubit, execute the optimization as illustrated in Fig. 3(b) to obtain the system-function parameters that characterize the IIR behavior of the low-temperature line accurately.

(4) For each qubit, employ the cryoscope method to measure the short-time-scale FIR response (approximately 20 ns) after correction by the IIR digital filter.

Next, we compare the run times of the time-domain characterization method and the optimization-based method. In Fig. 6(b), we sweep 100 different delay times, where the setting time of the response is about 600 ns. The run time approximates the total consumption time of the optimization-based method. However, time-domain characterization requires iterative calibration, which necessitates multiple measurements of the unit step response.

As a result, the optimization-based method outperforms time-domain characterization in terms of run time. Furthermore, the run time of the time-domain characterization is proportional to the time constant of the response. The longer the setting time of the response, the longer the time-domain characterization method will take. In contrast, for the optimization-based method, only the length of the RB sequence needs to be increased, without increasing the testing time.

[1] F. Arute, K. Arya, R. Babbush, D. Bacon, J. C. Bardin, R. Barends, R. Biswas, S. Boixo, F. G. Brandao, D. A. Buell *et al.*, Quantum supremacy using a programmable superconducting processor, Nature **574**, 505 (2019).

[2] Y. Wu, W.-S. Bao, S. Cao, F. Chen, M.-C. Chen, X. Chen, T.-H. Chung, H. Deng, Y. Du, D. Fan *et al.*, Strong quantum computational advantage using a superconducting quantum processor, Phys. Rev. Lett. **127**, 180501 (2021).

[3] Q. Zhu, S. Cao, F. Chen, M.-C. Chen, X. Chen, T.-H. Chung, H. Deng, Y. Du, D. Fan, M. Gong *et al.*, Quantum computational advantage via 60-qubit 24-cycle random circuit sampling, Sci. Bull. **67**, 240 (2022).

[4] J. C. Bardin, D. H. Slichter, and D. J. Reilly, Microwaves in quantum computing, IEEE J. Microw. **1**, 403 (2021).

[5] P. Krantz, M. Kjaergaard, F. Yan, T. P. Orlando, S. Gustavsson, and W. D. Oliver, A quantum engineer's guide to superconducting qubits, Appl. Phys. Rev. **6**, 021318 (2019).

[6] G. Burkard, T. D. Ladd, A. Pan, J. M. Nichol, and J. R. Petta, Semiconductor spin qubits, Rev. Mod. Phys. **95**, 025003 (2023).

[7] C. D. Bruzewicz, J. Chiaverini, R. McConnell, and J. M. Sage, Trapped-ion quantum computing: Progress and challenges, Appl. Phys. Rev. **6**, 021314 (2019).

[8] M. Saffman, Quantum computing with atomic qubits and Rydberg interactions: Progress and challenges, J. Phys. B: At., Mol. Opt. Phys. **49**, 202001 (2016).

[9] S. Gustavsson, O. Zwier, J. Bylander, F. Yan, F. Yoshihara, Y. Nakamura, T. P. Orlando, and W. D. Oliver, Improving quantum gate fidelities by using a qubit to measure microwave pulse distortions, Phys. Rev. Lett. **110**, 040502 (2013).

[10] Z. Chen, J. Kelly, C. Quintana, R. Barends, B. Campbell, Y. Chen, B. Chiaro, A. Dunsworth, A. Fowler, E. Lucero *et al.*, Measuring and suppressing quantum state leakage in a superconducting qubit, Phys. Rev. Lett. **116**, 020501 (2016).

[11] J. M. Martinis and M. R. Geller, Fast adiabatic qubit gates using only σ_z control, Phys. Rev. A **90**, 022307 (2014).

[12] S. Li, A. D. Castellano, S. Wang, Y. Wu, M. Gong, Z. Yan, H. Rong, H. Deng, C. Zha, C. Guo *et al.*, Realisation of high-fidelity nonadiabatic CZ gates with superconducting qubits, npj Quantum Inf. **5**, 1 (2019).

[13] J. Chu and F. Yan, Coupler-assisted controlled-phase gate with enhanced adiabaticity, Phys. Rev. Appl. **16**, 054020 (2021).

[14] B. Foxen, C. Neill, A. Dunsworth, P. Roushan, B. Chiaro, A. Megrant, J. Kelly, Z. Chen, K. Satzinger, R. Barends *et al.*, Demonstrating a continuous set of two-qubit gates for near-term quantum algorithms, Phys. Rev. Lett. **125**, 120504 (2020).

[15] X.-X. Yang, L.-L. Guo, H.-F. Zhang, L. Du, C. Zhang, H.-R. Tao, Y. Chen, P. Duan, Z.-L. Jia, W.-C. Kong *et al.*, Experimental implementation of short-path nonadiabatic geometric gates in a superconducting circuit, Phys. Rev. Appl. **19**, 044076 (2023).

[16] M. Rol, F. Battistel, F. Malinowski, C. Bultink, B. Tarasinski, R. Vollmer, N. Haider, N. Muthusubramanian, A. Bruno, B. Terhal *et al.*, Fast, high-fidelity conditional-phase gate exploiting leakage interference in weakly anharmonic superconducting qubits, Phys. Rev. Lett. **123**, 120502 (2019).

[17] J. Kelly, R. Barends, B. Campbell, Y. Chen, Z. Chen, B. Chiaro, A. Dunsworth, A. G. Fowler, I.-C. Hoi, E. Jeffrey *et al.*, Optimal quantum control using randomized benchmarking, Phys. Rev. Lett. **112**, 240504 (2014).

[18] A. V. Oppenheim, A. S. Willsky, and S. H. Nawab, *Signals and Systems* (Prentice-Hall International Ed., London, 1997).

[19] P. Cerfontaine, R. Otten, M. A. Wolfe, P. Bethke, and H. Bluhm, High-fidelity gate set for exchange-coupled singlet-triplet qubits, Phys. Rev. B **101**, 155311 (2020).

[20] M. A. Rol, L. Ciorciaro, F. K. Malinowski, B. M. Tarasinski, R. E. Sagastizabal, C. C. Bultink, Y. Salathe, N. Haandbaek, J. Sedivy, and L. DiCarlo, Time-domain characterization and correction of on-chip distortion of control pulses in a quantum processor, Appl. Phys. Lett. **116**, 054001 (2020).

[21] B. Foxen, J. Mutus, E. Lucero, E. Jeffrey, D. Sank, R. Barends, K. Arya, B. Burkett, Y. Chen, Z. Chen *et al.*, High speed flux sampling for tunable superconducting qubits with an embedded cryogenic transducer, Supercond. Sci. Technol. **32**, 015012 (2018).

[22] M. Jerger, A. Kulikov, Z. Vasselin, and A. Fedorov, *In situ* characterization of qubit control lines: A qubit as a vector network analyzer, Phys. Rev. Lett. **123**, 150501 (2019).

[23] B. R. Johnson, Ph.D. thesis, Department of Physics and Applied Physics, Yale University, 2011.

[24] M. Kjaergaard, M. E. Schwartz, J. Braumüller, P. Krantz, J. I.-J. Wang, S. Gustavsson, and W. D. Oliver, Superconducting qubits: Current state of play, Annu. Rev. Condens. Matter Phys. **11**, 369 (2020).

[25] Y. Salathé, P. Kurpiers, T. Karg, C. Lang, C. K. Andersen, A. Akin, S. Krinner, C. Eichler, and A. Wallraff, Low-latency digital signal processing for feedback and feedforward in quantum computing and communication, Phys. Rev. Appl. **9**, 034011 (2018).

[26] C. Guo, F. Liang, J. Lin, Y. Xu, L. Sun, W. Liu, S. Liao, and C. Peng, Control and readout software for superconducting quantum computing, IEEE Trans. Nucl. Sci. **66**, 1222 (2019).

[27] S. Palani, *Signals and Systems* (Springer International Publishing, Cham, 2022), p. 921.

[28] P. A. Lynn, *Electronic Signals and Systems* (Macmillan Education UK, London, 1986), p. 225.

[29] Z.-C. Xiang, K. Huang, Y.-R. Zhang, T. Liu, Y.-H. Shi, C.-L. Deng, T. Liu, H. Li, G.-H. Liang, Z.-Y. Mei *et al.*, Simulating Chern insulators on a superconducting quantum processor, Nat. Commun. **14**, 5433 (2023).

[30] R. Barends, J. Kelly, A. Megrant, A. Veitia, D. Sank, E. Jeffrey, T. C. White, J. Mutus, A. G. Fowler, B. Campbell *et al.*, Superconducting quantum circuits at the surface code threshold for fault tolerance, Nature **508**, 500 (2014).

[31] Y. Sung, L. Ding, J. Braumüller, A. Vepsäläinen, B. Kannan, M. Kjaergaard, A. Greene, G. O. Samach, C. McNally, D. Kim *et al.*, Realization of high-fidelity CZ and *ZZ*-free iSWAP gates with a tunable coupler, Phys. Rev. X **11**, 021058 (2021).

[32] V. K. Ingle and J. G. Proakis, *Digital Signal Processing Using* MATLAB (Cengage Learning, Stamford, Connecticut, 2012).

[33] F. Yan, P. Krantz, Y. Sung, M. Kjaergaard, D. L. Campbell, T. P. Orlando, S. Gustavsson, and W. D. Oliver, Tunable coupling scheme for implementing high-fidelity two-qubit gates, Phys. Rev. Appl. **10**, 054062 (2018).

[34] Y. Xu, J. Chu, J. Yuan, J. Qiu, Y. Zhou, L. Zhang, X. Tan, Y. Yu, S. Liu, J. Li *et al.*, High-fidelity, high-scalability two-qubit gate scheme for superconducting qubits, Phys. Rev. Lett. **125**, 240503 (2020).

[35] E. A. Sete, A. Q. Chen, R. Manenti, S. Kulshreshtha, and S. Poletto, Floating tunable coupler for scalable quantum computing architectures, Phys. Rev. Appl. **15**, 064063 (2021).

[36] C. Zhang, T.-L. Wang, L.-L. Guo, X.-Y. Yang, X.-X. Yang, P. Duan, Z.-L. Jia, W.-C. Kong, and G.-P. Guo, Characterization of tunable coupler without a dedicated readout resonator in superconducting circuits, Appl. Phys. Lett. **122**, 024001 (2023).

[37] J. M. Martinis, Superconducting phase qubits, Quantum Inf. Process. **8**, 81 (2009).

[38] R. Ma, B. Saxberg, C. Owens, N. Leung, Y. Lu, J. Simon, and D. I. Schuster, A dissipatively stabilized Mott insulator of photons, Nature **566**, 51 (2019).

[39] M. Hofheinz, H. Wang, M. Ansmann, R. C. Bialczak, E. Lucero, M. Neeley, A. O'connell, D. Sank, J. Wenner, J. M. Martinis *et al.*, Synthesizing arbitrary quantum states in a superconducting resonator, Nature **459**, 546 (2009).

[40] N. Wittler, F. Roy, K. Pack, M. Werninghaus, A. S. Roy, D. J. Egger, S. Filipp, F. K. Wilhelm, and S. Machnes, Integrated tool set for control, calibration, and characterization of quantum devices applied to superconducting qubits, Phys. Rev. Appl. **15**, 034080 (2021).

[41] E. Magesan, J. M. Gambetta, and J. Emerson, Scalable and robust randomized benchmarking of quantum processes, Phys. Rev. Lett. **106**, 180504 (2011).

[42] E. Magesan, J. M. Gambetta, and J. Emerson, Characterizing quantum gates via randomized benchmarking, Phys. Rev. A **85**, 042311 (2012).

[43] F. Motzoi, J. M. Gambetta, P. Rebentrost, and F. K. Wilhelm, Simple pulses for elimination of leakage in weakly nonlinear qubits, Phys. Rev. Lett. **103**, 110501 (2009).

[44] J. A. Nelder and R. Mead, A simplex method for function minimization, Comput. J. **7**, 308 (1965).

[45] Z. Li, P. Liu, P. Zhao, Z. Mi, H. Xu, X. Liang, T. Su, W. Sun, G. Xue, J.-N. Zhang *et al.*, Error per single-qubit gate below 10^{-4} in a superconducting qubit, Npj Quantum Inf. **9**, 111 (2023).

[46] E. Dogan, D. Rosenstock, L. Le Guevel, H. Xiong, R. A. Mencia, A. Somoroff, K. N. Nesterov, M. G. Vavilov, V. E. Manucharyan, and C. Wang, Two-fluxonium cross-resonance gate, Phys. Rev. Appl. **20**, 024011 (2023).

[47] J. M. Chow, L. DiCarlo, J. M. Gambetta, F. Motzoi, L. Frunzio, S. M. Girvin, and R. J. Schoelkopf, Optimized driving of superconducting artificial atoms for improved single-qubit gates, Phys. Rev. A **82**, 040305 (2010).